



**HAL**  
open science

# Non-classical nucleation of ordered L12 precipitates in the FCC based Al<sub>0.25</sub>CoFeNi high entropy alloy

Sriswaroop Dasari, Abhishek Sharma, Stéphane Gorsse, Advika Chesetti, Rajarshi Banerjee

► **To cite this version:**

Sriswaroop Dasari, Abhishek Sharma, Stéphane Gorsse, Advika Chesetti, Rajarshi Banerjee. Non-classical nucleation of ordered L12 precipitates in the FCC based Al<sub>0.25</sub>CoFeNi high entropy alloy. Journal of Applied Physics, 2023, 134 (1), pp.015102. 10.1063/5.0138924 . hal-04160302

**HAL Id: hal-04160302**

**<https://hal.science/hal-04160302>**

Submitted on 12 Jul 2023

**HAL** is a multi-disciplinary open access archive for the deposit and dissemination of scientific research documents, whether they are published or not. The documents may come from teaching and research institutions in France or abroad, or from public or private research centers.

L'archive ouverte pluridisciplinaire **HAL**, est destinée au dépôt et à la diffusion de documents scientifiques de niveau recherche, publiés ou non, émanant des établissements d'enseignement et de recherche français ou étrangers, des laboratoires publics ou privés.

# **Non-classical nucleation of ordered L<sub>12</sub> precipitates in the FCC based Al<sub>0.25</sub>CoFeNi high entropy alloy**

Sriswaroop Dasari<sup>a\*</sup>, Abhishek Sharma<sup>a</sup>, Stéphane Gorsse<sup>b</sup>, Advika Chesetti<sup>a</sup>, Rajarshi Banerjee<sup>a\*</sup>

<sup>a</sup> Department of Materials Science and Engineering, University of North Texas  
Denton, TX-76207, USA

<sup>b</sup> CNRS, Univ. Bordeaux, Bordeaux INP, ICMCB, UMR 5026, 33600 Pessac, France

\*Co-corresponding authors: [sriswaroop.dasari@unt.edu](mailto:sriswaroop.dasari@unt.edu), [raj.banerjee@unt.edu](mailto:raj.banerjee@unt.edu)

## **Abstract**

The complex interplay between competing phase stabilities of FCC, L<sub>12</sub>, BCC, and B2 phases in the Al<sub>0.25</sub>CoFeNi (7Al-31Co-31Fe-31Ni in at%) high entropy alloy (HEA), leads to non-classical phase transformation pathways and resultant novel microstructures. Specifically, the competition between homogenous precipitation of L<sub>12</sub> and heterogenous precipitation of BCC/B2 can be studied at a temperature of 500°C in Al<sub>0.25</sub>CoFeNi alloy. Upon isothermally annealing the single FCC phase microstructure of this HEA at 500°C up to 50 hours, the transformation initiates with the formation of a transient ordered L<sub>12</sub> phase with minor Ni-Al enrichment, which is far-from equilibrium, as revealed by atom probe tomography, and can be considered as non-classical nucleation. The near equilibrium L<sub>12</sub> phase eventually replaces the transient L<sub>12</sub> during continued annealing at the same temperature. However, the resultant FCC+L<sub>12</sub> microstructure is metastable because the true equilibrium for the Al<sub>0.25</sub>CoFeNi alloy at 500°C is a mixture of L<sub>12</sub>+B2 phases, as revealed by solution thermodynamics modeling. The higher nucleation barrier for the BCC-based ordered B2 phase coupled with the slower kinetics at 500°C, leads to the homogeneous precipitation of L<sub>12</sub>, while the B2 phase appears to sluggishly grow from grain boundaries acting as heterogeneous nucleation sites.

**Keywords:** High entropy alloy, Phase transformation pathway, Non-classical nucleation, Ordered L1<sub>2</sub>, Ordered B2

## 1. Introduction

Phase transformation pathways are critical in achieving the true equilibrium of an alloy. The processing conditions as well as the prior history of the alloy dictates the pathway for a phase transformation. For example, applied stress or prior deformation can accelerate the equilibrium phase formation especially in case of phases with high nucleation barrier<sup>1-4</sup>. When the time and/or temperature is insufficient, the alloy can form a metastable microstructure to relieve the supersaturation<sup>5</sup>. Irradiation can also accelerate the kinetics of phase transformation<sup>6-9</sup>. In any case, the parent microstructure is a supersaturated solid solution, and the product is the equilibrium microstructure but the pathway from parent to product can change depending on the imposed conditions. While these are kinetic limitations, the pathway is also dependent more importantly on the thermodynamic driving force for the transformation. The driving force of the system is determined by the free-energy hypersurface in a multi-dimensional compositional and structural space, i.e., the transformation would follow the minimum energy path (MEP)<sup>10</sup> on the free energy surface if all degrees of freedom of atomic rearrangements including diffusional and diffusionless paths (shear and shuffle for example) are accessible. However, if some of the degrees of freedom (e.g., solute partitioning by long range diffusion) are limited by the kinetics, then the actual transformation path may deviate from the MEP. The driving force for transformation arises from interaction energies among elements and the configurational entropy. Therefore, high entropy

alloys which exhibit a wide range of interaction energies among constituent elements <sup>11,12</sup> and high configurational entropy are ideal candidates to investigate new phase transformation pathways.

High entropy alloys (HEAs) or Complex concentrated alloys (CCAs), recently introduced by Cantor <sup>13</sup> and Yeh <sup>14</sup> contain multiple elements in high concentrations, as opposed to one principal element. Although these alloys were initially introduced as single-phase solid solutions, multi-phase microstructures have also been possible when elements with strong ordering/clustering tendencies formed the alloy <sup>5,15,16</sup>. In fact, research over past decade has largely been focused on multi-phase HEAs <sup>15,17-22</sup>. The current study is also focused on such an alloy with the composition Al<sub>0.25</sub>CoFeNi. The high negative enthalpy of mixing between Al and Ni leads to a strong ordering tendency in this alloy which could not be suppressed during solutionizing and water quenching consequently leading to the formation of short-range ordered domains <sup>16</sup>. This ordering tendency also leads to various multi-phase fields as reported previously <sup>23</sup>. Two distinct microstructures, FCC+B2 and FCC+L1<sub>2</sub>+BCC+B2 were reported in this alloy <sup>23</sup>. The latter four-phase microstructure is a nano-lamellar structure that exhibits excellent strength-ductility combination <sup>23</sup>. The phase stability in Al<sub>0.25</sub>CoFeNi alloy warrants further investigation because it can provide insights into the implications of ordering tendency on phase transformation pathways. In the current study, the phase stability and microstructural evolution upon isothermal annealing of Al<sub>0.25</sub>CoFeNi at 500°C up to 50 hours was investigated. Specifically, 500°C temperature was chosen to provide thermal activation for investigating the evolution of short-range ordered domains previously reported in the solutionized condition <sup>16</sup>.

## **2. Methods and Materials**

Based on the thermodynamic binary enthalpies of mixing as listed in Table 1<sup>24</sup>, a base three-component alloy was chosen such that the solid solution closely resembles a random solid solution. The chosen composition is CoFeNi, since the interaction energies of the binary pairs within this ternary system i.e., Co-Fe, Fe-Ni, Ni-Co, are nearly equal to zero, making this a near ideal solid solution. Subsequently, ~8 at% Al was added to CoFeNi to intentionally introduce an ordering tendency. The primary elements that participate in chemical ordering within the random solid solution are Ni and Al which have the most negative binary mixing enthalpy.

Table 1: Enthalpy of mixing (kJ/mol) of the binary liquids at equi-atomic composition<sup>24</sup>.

<b>Element</b>	<b>Al</b>	<b>Fe</b>	<b>Co</b>	<b>Ni</b>
<b>Al</b>	-	-11	-19	-22
<b>Fe</b>	-	-	-1	-2
<b>Co</b>	-	-	-	0
<b>Ni</b>	-	-	-	-

Al<sub>0.25</sub>CoFeNi, with the nominal chemical composition 8.4Al-30.3Co-30.3Fe-30.3Ni (at. %) was procured from ACI alloys Inc. The actual composition of the ingot measured with Scanning Electron Microscope – Energy Dispersive Spectroscopy (SEM-EDS) is 8.5Al-30.8Co-30.6Fe-30.1Ni (at. %). The SEM-EDS measurements were performed across five different regions of 2.6×2.2 mm<sup>2</sup> area and then averaged. The cast alloy was homogenized at 1200°C for 1 hr prior to rolling and annealing treatments. The homogenized alloy was subjected to 90% reduction in thickness via cross rolling. The cold rolled plate was subsequently annealed at 1200°C for 5 min

to obtain single-phase FCC solid solution, with recrystallized grains of average size ~100 nm. This condition will be referred to as the solutionized condition. The solutionized samples were then subjected to isothermal annealing either at 500°C for 0.5, 2, 5, 10 and 50 hrs. The nomenclature used for these conditions is 500C/X (X = 30 min, 2 hrs, 5 hrs, 10 hrs, 50 hrs) for samples annealed at 500°C. The cold rolled specimens were encapsulated in stainless steel foil for all heat treatments and water quenched.

Microstructural characterization was performed with FEI Nova-NanoSEM 230™ scanning electron microscope (SEM) fixed with Hikari Super electron backscattered diffraction (EBSD) detector and FEI Tecnai G2 TF20™ Transmission electron microscopy (TEM) operating at 200 kV. TEM lift-outs were prepared using an FEI Nova 200 dual beam focused ion beam (FIB) microscope. A TEM lift-out of dimensions ~15x2x5 μm was initially prepared with the help of the omniprobe micromanipulator in FIB. This 2 μm thick sample was subsequently thinned to dimensions ~50-100 nm in multiple steps by progressively reducing the voltage and/or current of the Ga ion beam in the dual-beam FIB. Cameca Local Electrode Atom Probe (LEAP 5000XS) instrument was used in the current study to obtain detailed compositional information. The APT instrument was operated at a temperature of 30 K, pulse rate of 200 kHz, and a detection rate of 0.005-0.01 ion/pulse in laser mode with laser pulse energy of 50 nJ. AP Suite 6 software was used to analyze the APT data. The mass spectrum for APT reconstructions was calibrated based on the bulk compositions obtained from SEM-EDS. H and Ga contamination from APT chamber and FIB have not been indexed in the mass spectrum for comparison purposes.

Mechanical properties were measured in a customized mini-tensile testing machine at a strain rate of 0.001/sec, which used a linear variable displacement transformer (LVDT) extensometer. Tensile specimens with approximate gauge dimensions  $5 \times 1 \times 1$  mm were sectioned in an Electric Discharge Machine. Three specimens were tested for each condition for statistical accuracy.

### 3. Results

#### *Thermodynamic Modeling*

An isopleth for the  $Al_xCoFeNi$  system with varying Al content in CoFeNi was calculated using a solution thermodynamic based CALPHAD approach using the Thermocalc software and employing the TCHEA3 database and is shown in Fig. 1(a). Based on this isopleth that can be treated as a pseudo-binary section of the complex multi-component phase diagram, the composition of  $Al_{0.25}CoFeNi$  was chosen since this composition traverses a large range of different complex multi-phase fields, involving combinations of long-range ordered (LRO) phases as well as disordered solid solution phases. These phase-fields include  $L1_2$  (LRO of FCC structure) + B2 (LRO of BCC), FCC (disordered) +  $L1_2$  + B2, and FCC + B2. The predicted phase stability for the composition  $Al_{0.25}CoFeNi$  at  $500^\circ C$  is a two-phase  $L1_2$  + B2 field. The phase fraction vs temperature plot is also given in Fig. 1(b) for estimating the predicted equilibrium phase fractions. However, it must be noted that while the predictions afforded by such solution thermodynamic models of concentrated multi-component systems are a good guideline, there are inaccuracies in associated databases affecting the accuracy of the predictions, as reported previously<sup>23</sup>.

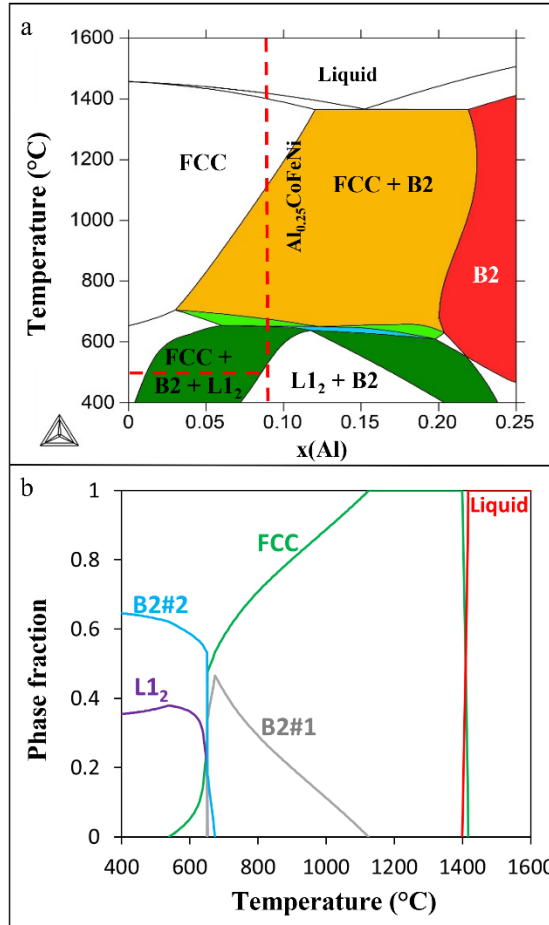


Figure 1: (a) Pseudo-binary isopleth of varying Al in ternary CoFeNi system (b) Phase fraction vs temperature plot for the  $\text{Al}_{0.25}\text{CoFeNi}$  alloy <sup>23</sup>.

### ***Detailed microstructural characterization of solutionized and 500°C annealed conditions***

The results from microstructural characterization of solutionized condition, as reported previously <sup>16</sup> are shown in Fig. 2. The SEM backscattered micrograph in Fig. 2(a) shows a coarse grain single-phase microstructure. The selected area electron diffraction pattern (SAEDP) in Fig. 2(b) shows reflections consistent with single FCC phase. Further, the APT raw ion maps of all elements in Figs. 2 (c-f) show a homogenous distribution of elements at this scale. However, examining the elemental distributions within the volume represented by the black rectangle in Fig. 2(f) using frequency distribution analyses indicated a departure from randomness in this alloy. Solute clustering algorithm <sup>25,26</sup> of the APT data revealed Ni-Al rich clusters as shown in Fig. 2(g) with

an average composition of 50Ni-15Al-18Fe-17Co at.% Al. Though the TEM results from this condition indicate absence of secondary phases or LRO, APT results reveal Ni-Al rich domains, uniformly distributed within the FCC solid solution<sup>16</sup>. The formation of these Ni-Al rich domains within the FCC solid solution can be attributed to the large negative enthalpy of mixing for binary Ni-Al, which has a larger magnitude as compared to Fe-Al and Co-Al interactions<sup>9</sup>. While the nature of ordering within these Ni-Al rich domains cannot be confirmed solely based on these APT and TEM results, it is possible that these are short-range ordered (SRO) domains which have been reported in multiple high entropy alloys<sup>27-30</sup>. These SRO domains are the predecessors of LRO domains/precipitates that form in this alloy on subsequent isothermal annealing at 500°C.

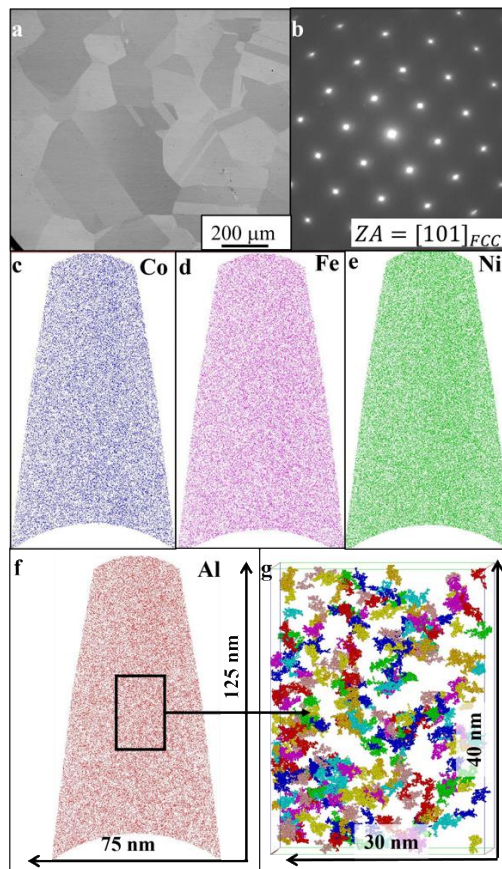


Figure 2: Microstructural characterization of solutionized condition. (a) SEM micrograph showing a single-phase microstructure. (b) SAEDP pattern obtained from [101] zone axis of  $\text{Al}_{0.25}\text{CoFeNi}$  reveals single FCC phase microstructure. APT raw ion maps of (c) Co (d) Fe (e) Ni and (f) Al. (g)

3D reconstruction of Ni-Al rich clusters obtained via cluster analysis. The clusters are represented with different colors.

The TEM and APT results from 500C/30min condition are shown in Fig. 3. The selected area electron diffraction pattern (SAEDP) in Fig. 3(a) shows faint and diffuse superlattice reflections at  $\{001\}$  positions in addition to the FCC fundamental spots. This indicates the presence of early stage LRO domains in the FCC matrix, as also revealed by the dark-field micrograph in Fig. 3(b). Interestingly, a  $\sim 2$  nm thick two-dimensional (2D) section of the three-dimensional (3D) Al and Fe ion maps obtained from APT, shown in Figs. 3(c-d) do not exhibit any obvious chemical partitioning in the FCC matrix. Co and Ni raw ion maps are shown in supplementary Fig. S1. However, investigating the local distribution of individual elements using frequency distribution analysis reveals non-randomness in the FCC solid solution. Based on this evidence, cluster analysis was performed, and the resultant distribution of these clusters is shown in Fig. 3(e). The Ni-Al enrichment and volume fraction of these clusters show a marginal increase compared to the quenched condition.

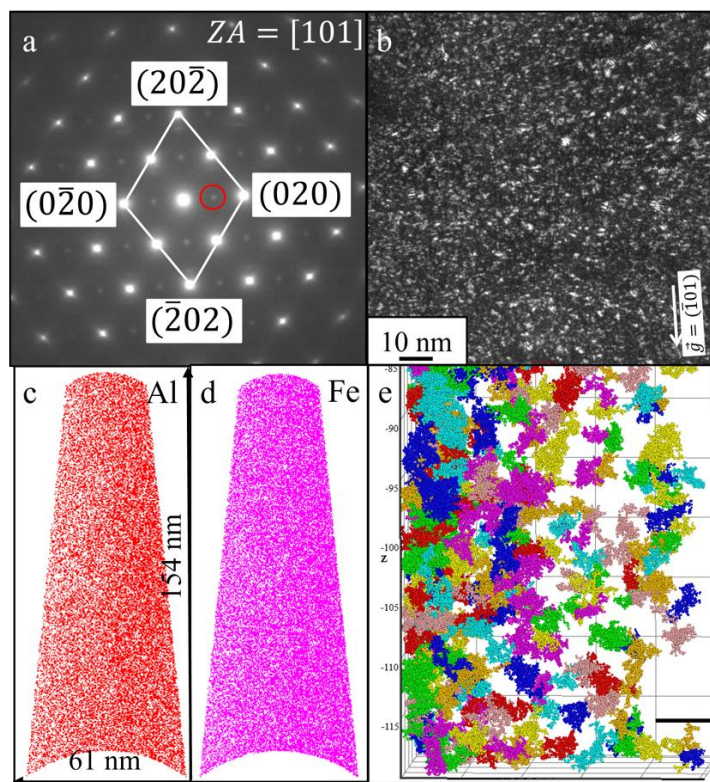


Figure 3: TEM and APT of 500C/30min condition. (a) Diffraction pattern showing faint superlattice reflections at  $\{001\}$  positions indicating early stage  $L1_2$  ordering (b) Dark-field micrograph from one of the superlattice reflections in (a); (c-d) Al and Fe ion maps obtained from APT. Co and Ni maps are in supplementary Fig. S1 (e) Distribution of Ni-Al rich domains as revealed by cluster analysis. The clusters are represented with different colors.

Increasing the annealing time to 2 hrs leads to the formation of  $\sim 7$  nm  $L1_2$  precipitates. The TEM and APT results from 500C/2hrs are shown in Figs. 4(a-d). The SAEDP in Fig. 4(a) also shows the presence of  $L1_2$  superlattice reflections, similar to those observed in case of the 500C/30min condition. Relatively coarse  $L1_2$  precipitates  $\sim 7$  nm can be observed in the dark field micrograph in Fig. 4(b). The Al ion map along with Al  $\sim 15$  at.% iso-concentration surface in Fig. 4(c) shows a sparse distribution of spherical/ellipsoidal  $L1_2$  precipitates in the FCC matrix. All raw ion maps are in supplementary Fig. S1. The proximity histogram or proxigram<sup>31</sup> constructed across the Al 15 at.% iso-surface (Fig. 4(d)) shows the average compositional partitioning of all the elements across all the precipitate/matrix interfaces.

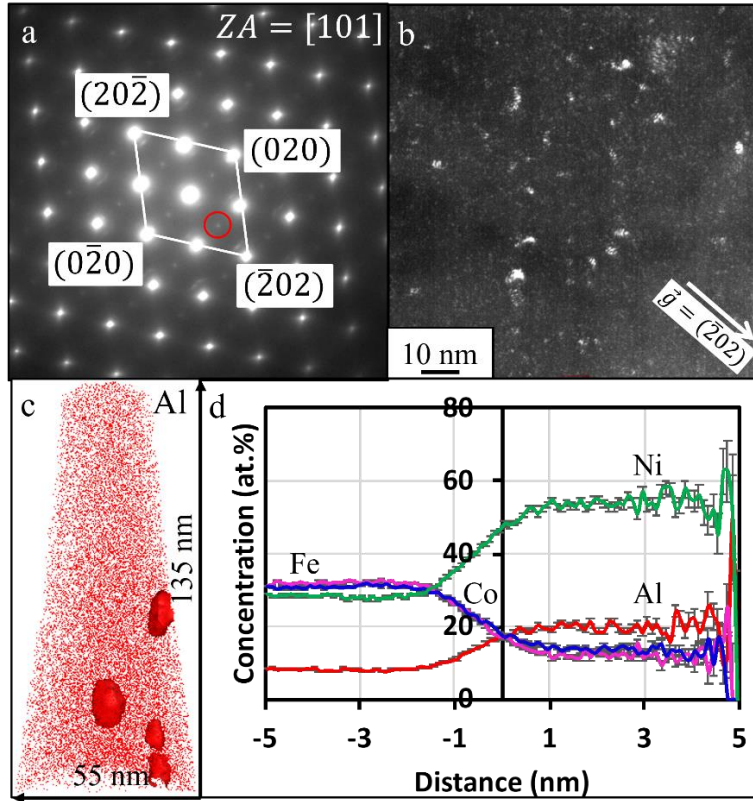


Figure 4: TEM and APT of 500C/2hrs condition (a) Diffraction pattern showing  $\{001\}$  superlattice reflections (b) Dark-field micrograph from one of the superlattice reflections in (c) showing sparse distribution of  $L_{12}$  precipitates (d) Al ion map with Al 15 at.% iso-surface showing spherical/ellipsoidal  $L_{12}$  precipitates. All raw ion maps are in supplementary Fig. S1 (e) Proxigram constructed across Al 15 at.% iso-surface showing compositional partitioning between the matrix and precipitates.

Figs. 5 (a-d) shows the TEM and APT results from 500C/10hrs condition. The SAEDP obtained from  $\{001\}$  zone axis showing the superlattice reflections is included in Fig. 5(a). The dark field micrograph obtained from a superlattice reflection in Fig. 5(b) reveals the well-developed  $L_{12}$  precipitates. The Al ion map superimposed with Al 14.1 at.% iso-surface in Fig. 5(c) reveals a relatively high density of  $L_{12}$  precipitates in this condition. All raw ion maps are in supplementary Fig. S2. The proxigram constructed across Al 14.1 at.% iso-surface in Fig. 5(d) shows the compositional partitioning in 500C/10hrs condition.

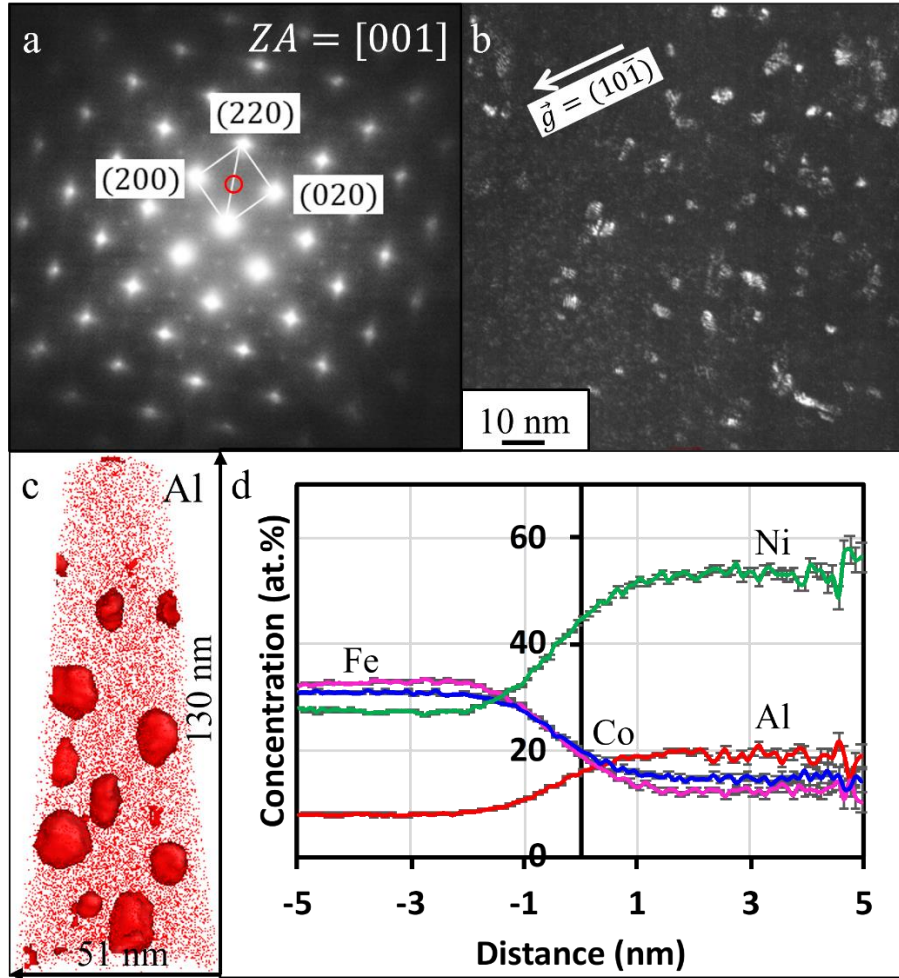


Figure 5: (a-d) TEM and APT of 500C/10hrs condition. (a) Diffraction pattern showing superlattice reflections at  $\{001\}$  positions indicating L12 ordering (b) Dark-field micrograph from one of the superlattice reflections in (a); (c) Al ion map along with Al 14.1 at.% iso-surface obtained from APT. All raw ion maps are in supplementary Fig. S2 (d) Proxigram constructed across Al 14.1 at.% iso-surface showing compositional partitioning between the matrix and precipitates.

Finally, Figs. 6(a-d) shows the TEM and APT results from 500C/50hrs condition. The SAEDP shown in Fig. 6(a) reveals sharp superlattice reflections. The dark-field micrograph in Fig. 6(b) shows a relatively lower number density but larger precipitates in this condition. In agreement, the Al ion map superimposed with Al 14.7 at.% iso-surface in Fig. 6(c) reveals few  $\sim 30$  nm L1<sub>2</sub> precipitates in this condition. All raw ion maps are in supplementary Fig. S2. The proxigram

constructed across Al 14.7 at.% iso-surface in Fig. 6(d) shows the compositional partitioning across the precipitate/matrix interface in 500C/50hrs condition.

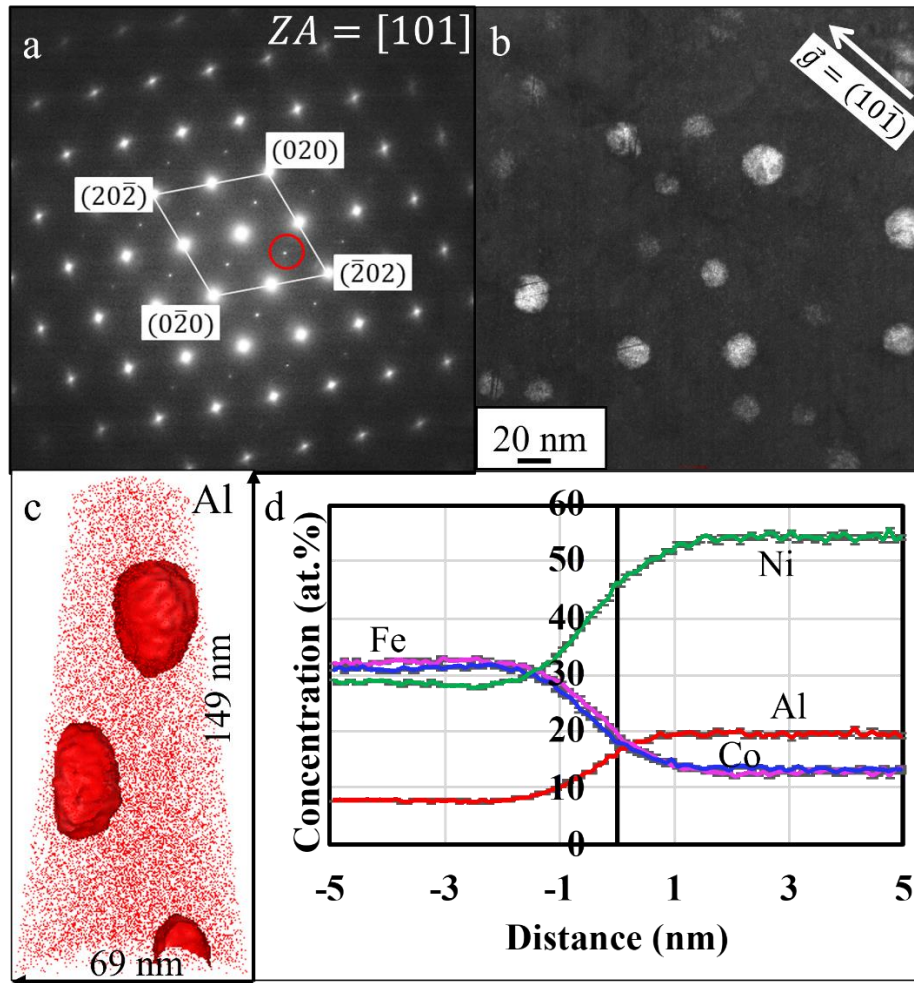


Figure 6: TEM and APT of 500C/50hrs condition (a) Diffraction pattern showing sharp  $\{001\}$  superlattice reflections (b) Dark-field micrograph from one of the superlattice reflections in (a) showing  $L1_2$  precipitates (c) Al ion map with Al 14.7 at.% iso-surface showing spherical/ellipsoidal  $L1_2$  precipitates. All raw ion maps are in supplementary Fig. S2 (d) Proxigram constructed across Al 14.7 at.% iso-surface showing compositional partitioning between the matrix and precipitates.

While the microstructure in 500C/50hrs condition is largely FCC+ $L1_2$ , there is a competing transformation taking place at the grain boundaries as shown in Figs. 7(a-b). TEM diffraction analysis from the grain boundary product revealed reflections consistent with either a fully B2 phase or a mixture of BCC and B2 phases, with all the fundamental BCC reflections overlapping

with the B2 reflections. This product is restricted to grain boundaries due to the high nucleation barrier for precipitation within the FCC matrix, and slower kinetics at 500°C. Further detailed investigation of this grain boundary product is underway. However, since the B2 is an equilibrium phase at this temperature, the metastable FCC+L1<sub>2</sub> microstructure is expected to be eventually replaced by the equilibrium L1<sub>2</sub>+B2 microstructure.

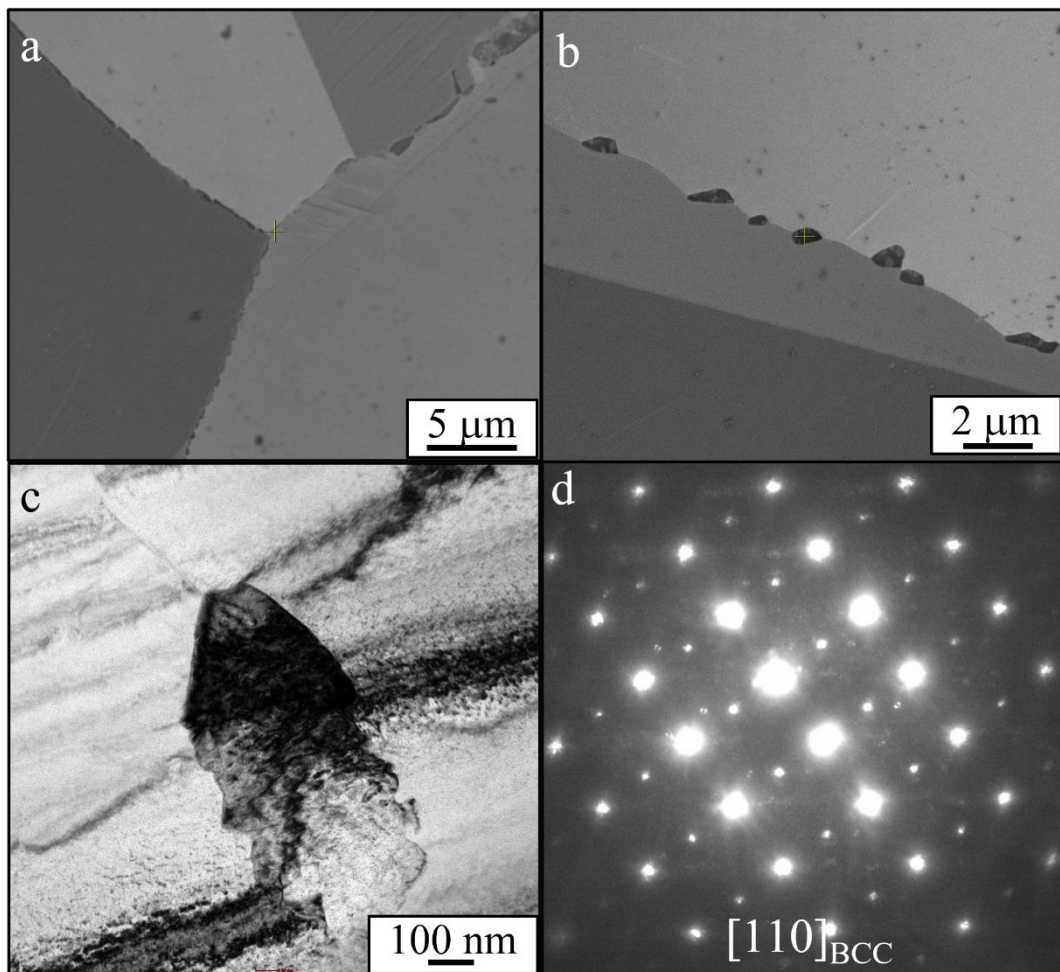


Figure 7: (a-b) Backscattered SEM images from 500C-50 hrs condition showing growth of lamellar colonies from grain boundaries (c) TEM bright field image showing one such colony at a grain boundary (d) Diffraction pattern recorded from the colony in (c) can be consistently indexed as B2 structure indicating that the colony contains either B2 or both BCC and B2 phases.

#### 4. Discussion

##### *Phase Transformation Pathways*

The simple quaternary  $\text{Al}_{0.25}\text{CoFeNi}$  alloy is a good candidate system for investigating the interplay of multiple competing phase transformation pathways in concentrated multi-component alloys. Isothermal annealing at  $500^\circ\text{C}$  revealed an interesting and rather unusual phenomenon where two  $\text{L}_{12}$  phases (with different compositions) formed in the same alloy co-existed in the same alloy. This condition of co-existence of  $\text{L}_{12}$  precipitates of two distinctly different compositions, represent two stages of evolution of the same  $\text{L}_{12}$  phase.

The role of alloying elements, such as Al and Ti, on the departure from randomness in the FCC solid solution in case of 3d transition element based HEAs/CCAs such as CoFeNi has been discussed in previous papers<sup>16,17</sup>. Such a departure from randomness results from the introduction of a certain degree of chemical ordering in the FCC solid solution, as manifested in case of the  $\text{Al}_{0.25}\text{CoFeNi}$  alloy, wherein nano scale Ni-Al rich clusters were observed in APT results from the solutionized and quenched condition<sup>16</sup>. These Ni-Al rich domains are a result of compositional fluctuations resulting from the strong negative enthalpy of mixing for Ni-Al, substantially stronger than the competing Fe-Al and Co-Al interactions (refer to Table 1). These compositional fluctuations presumably lead to local SRO domains within the FCC solid solution, though the results presented in this paper preclude a conclusive determination of the ordering state within these nanometer sized clusters. Furthermore, these clusters are likely to have formed either at the solutionizing temperature of  $1200^\circ\text{C}$ , or during the quenching. Subsequent isothermal annealing at  $500^\circ\text{C}$  leads to the evolution of these Ni-Al rich clusters into LRO  $\text{L}_{12}$  precipitates within the FCC matrix, as observed in case of the  $500^\circ\text{C}/30\text{min}$  condition. TEM results showed the presence of diffuse superlattice  $\{001\}$  type spots indicative of LRO domains, exhibiting  $\text{L}_{12}$  type ordering. However, APT results did not exhibit any discrete compositionally partitioned domains (not

detectable by iso-surfaces), although minor changes in the composition and volume fraction of Ni-Al rich domains are observed, based on cluster analysis, similar to those observed in the solutionized condition. These LRO L<sub>12</sub> domains/nano-precipitates appear to be a transient ordered phase forming from the pre-existing Ni-Al rich compositional fluctuations (presumably SRO domains) in case of the solutionized condition. The composition of these transient LRO L<sub>12</sub> domains, is close to those of the Ni-Al rich clusters in the solutionized condition, but somewhat different from the discrete L<sub>12</sub> precipitates which appear after 2hrs annealing at 500°C (refer to Table 2). Therefore, these transient LRO domains are likely to have resulted from congruent (or with minimal diffusional partitioning) transformation of the pre-existing Ni-Al rich clusters. Traditionally, in a classical nucleation and growth process, it is widely accepted that a nucleus of the precipitating phase (including ordered phases) of near equilibrium composition is directly formed within the parent matrix<sup>32</sup>. Since the Ni-Al rich domains present in the solutionized condition, are likely to have transformed into LRO L<sub>12</sub> domains during the early stages of annealing, via a congruent transformation, their compositions are far-from the equilibrium composition. This pathway can be considered a non-classical nucleation and growth pathway for L<sub>12</sub> precipitation in the Al<sub>0.25</sub>CoFeNi HEA.

Further increase in annealing time to 2 hrs led to a sparse distribution of discretely identifiable L<sub>12</sub> precipitates, based on both dark-field TEM images as well as Al-rich iso-surfaces in APT reconstructions. These discrete well-developed L<sub>12</sub> precipitates exhibit distinctly different compositions, with ~4at% higher Al content, as compared to the transient L<sub>12</sub> nanodomains forming at the early stages of annealing. These well-developed L<sub>12</sub> precipitates are likely to have grown from the pre-existing far-from equilibrium transient L<sub>12</sub> nanodomains by rejecting Co and

Fe, while getting enriched in Al. This progressively pushes their composition closer to equilibrium at 500°C, as observed in the results listed in Table 2. The precipitate size, number density and composition for different isothermal annealing times, are listed in Table 2.

Table 2: The variation in size, number density and composition of ordered domains with aging time.

<b>Condition</b>	<b>Domain size</b>	<b>Number density (<math>\mu\text{m}^{-3}</math>)</b>	<b>Composition (at. %)</b>
Quenched	~2 nm	$6.3 \times 10^6$	14.9Al-50.4Ni-17.5Co-17.2Fe
500°C-30 min	~2 nm	$5.7 \times 10^6$	16.3Al-52.3Ni-15.3Fe-16.1Fe
500°C-2 hrs	~7 nm	$2.0 \times 10^4$	19.6Al-54Ni-13.2Fe-13.2Co
500°C-10 hrs	~10 nm	$8.6 \times 10^4$	20Al-53Ni-13.9Co-13.1Fe
500°C-50 hrs	~35 nm	$0.67 \times 10^4$	20.1Al-53.9Ni-13Co-13Fe

It is interesting to note that the number density of  $L_{12}$  precipitates appears to drastically decreases from 500C/30min condition to 500C/2hrs condition. This is because the transient  $L_{12}$  nanodomain in case of the 500C/30min condition are gradually evolving into near equilibrium  $L_{12}$  precipitates, accompanied by a change in composition. Since the equilibrium  $L_{12}$  precipitates contain substantially higher Al as compared to the transient  $L_{12}$  nanodomains, solute conservation dictates that the growth of the equilibrium precipitates is only possible via reduction in the number of transient  $L_{12}$  nanodomains. Consequently, in case of the 500°C/2hr annealed condition, it is expected that the regions away from the larger equilibrium  $L_{12}$  precipitates will contain remnants of the original transient  $L_{12}$  nanodomains. Therefore, using the APT results, cluster analysis was

performed on the 500C/2hrs reconstruction away from the discrete well-developed L1<sub>2</sub> precipitates, to explore the possible presence of Ni-Al rich clusters. These results are summarized in Fig. 8. The Al ion map with Al 15 at.% iso-surface in Fig. 4(c) is reproduced in Fig. 8(a) and the volume (20×20×30 nm<sup>3</sup>) used for cluster analysis is shown using the solid rectangle. The concentration profiles as a function of distance (radius) i.e. radial distribution curves with center atoms as either Fe or Co are shown in Fig. 8(b). These curves show that Fe and Co tend to be preferred neighbors in agreement with Fe-Co rich matrix, and Ni-Al rich clusters. The cluster analysis reveals the presence of Ni-Al rich clusters, as shown in Fig. 8(c). The average cluster radius and volume fraction are 1.54 nm and 6.6 respectively. The average Al and Ni concentration in these clusters are ~15.7 at.% and ~53.6 at.% respectively similar to solutionized and 500°C/30mins conditions while the number density of these clusters is 4.3 x 10<sup>6</sup> μm<sup>3</sup> is significantly lower than those observed in the solutionized and 500°C/30mins annealed conditions. Therefore, after annealing for 2hrs this HEA exhibits the co-existence of two types of L1<sub>2</sub> domains, the larger scale well-developed L1<sub>2</sub> precipitates with discrete interfaces and compositions close to equilibrium (Fig. 8(a)) and the finer scale transient L1<sub>2</sub> nanodomains arising from the pre-existing small-scale Ni-Al rich compositional fluctuations (presumably SRO domains), exhibiting far-from equilibrium compositions (Fig. 8(c)).

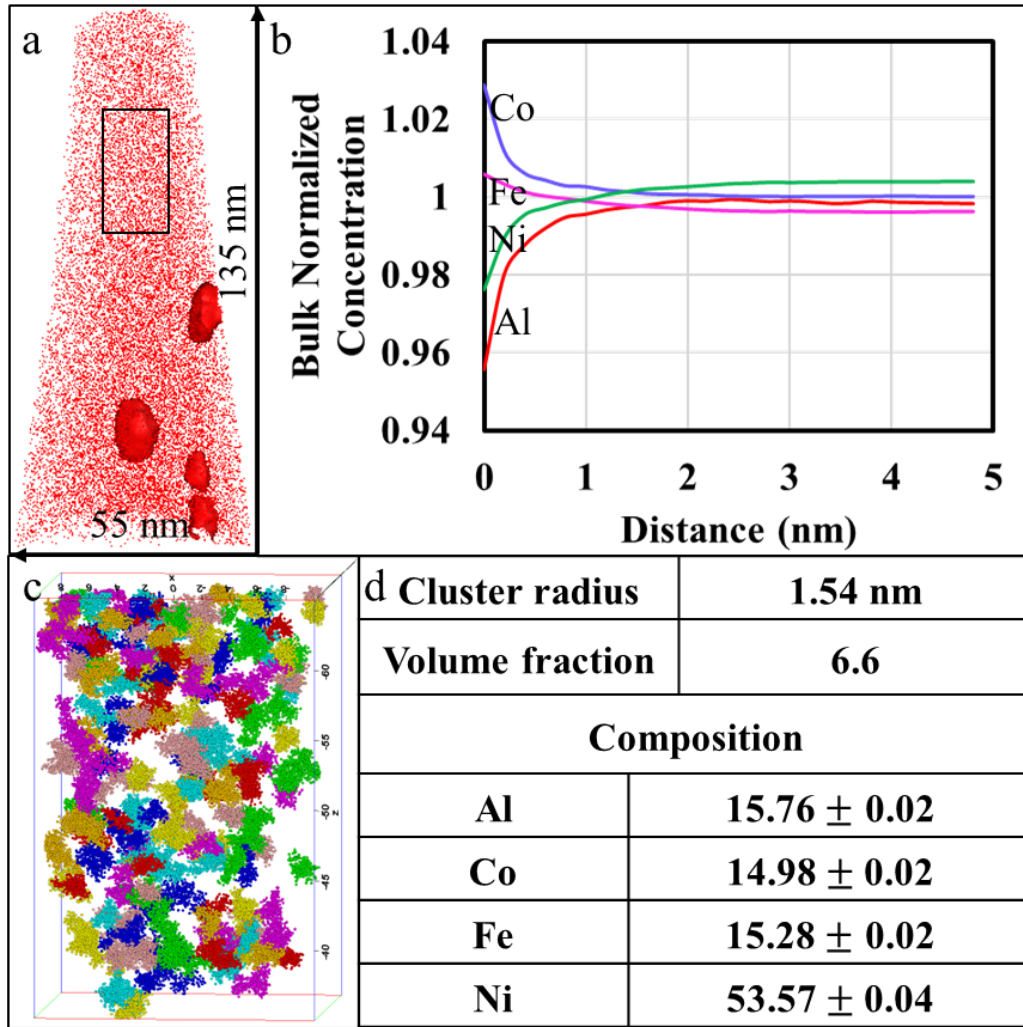


Figure 8: (a) Al ion map with Al 15 at.% iso-surface reproduced from Fig. 4(c) but overlaid with the volume (solid rectangle) used for cluster analysis. (b) Radial distribution curves show the evidence for Fe-Co, and Ni-Al preferential clustering. (c) Distribution of Ni-Al rich domains as revealed by cluster analysis. (d) The average radius, volume fraction and composition of Ni-Al rich clusters in 500C/2hrs condition.

Upon further annealing, the number density of the discrete well-developed  $L_{12}$  precipitates increased with annealing time up to 10 hrs and later decreased in case of the 500°C/50hrs condition. Based on the trend in number density of well-developed near-equilibrium  $L_{12}$  precipitates, the growth stage of these precipitates is expected to lie in between 2 hrs and 10 hrs, followed by coarsening between 10 hrs and 50 hrs of annealing. The domain/precipitate size in each of the conditions are as follows: ~2 nm in solutionized condition, ~2 nm in 500°C/30min, ~7

nm in 500°C/2hrs, ~10 nm in 500°C/10hrs and ~35 nm in 500°C/50hrs. The approximate Ni and Al content (in at.%) of the domains/precipitates with annealing time are as follows: 15Al-50Ni in solutionized, 16Al-52Ni in 500°C/30min, 20Al-54Ni in 500°C/2hrs, 20Al-53Ni in 500°C/10hrs and 20Al-54Ni in 500°C/50hrs. This information is also tabulated in Table 2.

Concurrently with the L1<sub>2</sub> precipitation, the nucleation and growth of B2 phase was observed along grain boundaries (refer to Fig. 7). The predicted equilibrium phase-field for this composition (refer to Fig. 1) at 500°C is L1<sub>2</sub> + B2. The ordered L1<sub>2</sub> phase is ordering based on a parent FCC lattice and forms a low energy FCC/L1<sub>2</sub> interface. Consequently, there is a low nucleation barrier for homogeneous nucleation of the L1<sub>2</sub> domains/precipitates, allowing for the uniform intragranular nucleation and growth of these precipitates. In contrast, the ordered B2 phase is based on ordering on a parent BCC lattice and forms a relatively high energy FCC/B2 interface. Consequently, the energy barrier for B2 nucleation in the FCC matrix is very high, leading to heterogeneous nucleation at the FCC grain boundaries. The underlying details have been previously discussed [3,16]. Interestingly, no L1<sub>2</sub> precipitation was observed at the grain boundaries. Fig. 9 shows the onset driving forces for L1<sub>2</sub> and B2 phases as a function of temperature calculated using ThermoCalc TCHEA3 database<sup>23</sup>. The grain boundaries which are heterogenous nucleation sites aid in nucleating the B2 phase which has substantially higher driving force than L1<sub>2</sub> phase. Furthermore, precipitation of B2 along grain boundaries will lead to a local depletion of Al and Ni in the FCC matrix in the vicinity of the boundary, resulting in little supersaturation, or very limited driving force, for subsequent L1<sub>2</sub> precipitation at the grain boundary. However, after nucleation, the growth kinetics of B2 phase appears to be very sluggish due to low diffusivity at the low temperature (500°C), and the interfacial and strain energies acting against the thermodynamic

chemical driving force for B2 precipitation. Nevertheless, it is likely that after sufficiently long annealing times, possibly on the order of hundreds of hours at 500°C, an equilibrium microstructure with only L1<sub>2</sub> and B2 phases might dominate, as opposed to the dominant FCC+L1<sub>2</sub> microstructure after 500°C/50 hrs of annealing.

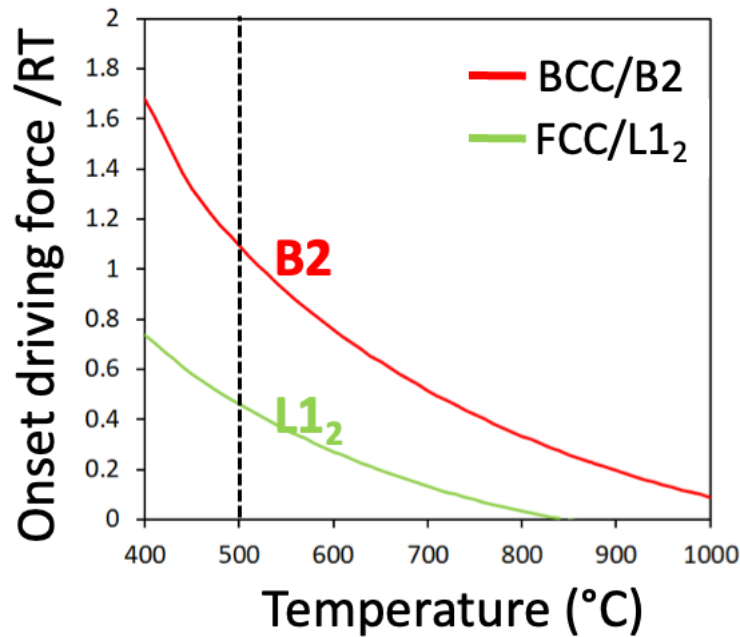


Figure 9: The onset driving forces for L1<sub>2</sub> and B2 phases as a function of temperature calculated using TCHEA3 database in ThermoCalc <sup>23</sup>.

### *Microhardness and tensile properties*

The microhardness values obtained from all the conditions are given in Figure 10(a), and clearly reveal a distinct difference in the strengthening effect of the early stage far-from equilibrium transient L1<sub>2</sub> nanodomains versus the well-developed discrete near-equilibrium L1<sub>2</sub> precipitates. Thus, the microhardness values are substantially lower for annealing times of 0 hrs, 0.5 hrs (30 mins), and 2 hrs, as compared to those for 5 hrs, 10 hrs, and 50 hrs. This indicates that the early stage far-from equilibrium transient L1<sub>2</sub> nanodomains are not as effective strengtheners presumably due to their smaller change in composition as compared to the FCC matrix, leading to

smaller misfits and lower coherency stresses. In contrast, the well-developed discrete  $L1_2$  precipitates are expected to have a higher misfit and consequently higher coherency stresses, leading to higher strengths. Comparing the microstructures of the 500°C/30mins versus the 500°C/2hrs annealed conditions, while there are a limited number of well-developed equilibrium (or near equilibrium)  $L1_2$  precipitates in the latter case, the predominant fraction in both cases comprise the transient  $L1_2$  nanodomains. Therefore, in both cases the microhardness is dominated by these transient  $L1_2$  nanodomains and are consequently very similar. However, due to the co-existence of both well-developed  $L1_2$  precipitates as well as transient  $L1_2$  nanodomains in case of the 500°C/2hrs annealed sample, there is a larger statistical variation in the microhardness value, as reflected in the larger error bar (Fig. 10(a)). Thus, regions with a higher local fraction of well-developed  $L1_2$  precipitates presumably exhibit a higher microhardness as compared to those regions locally dominated by the transient  $L1_2$  nanodomains.

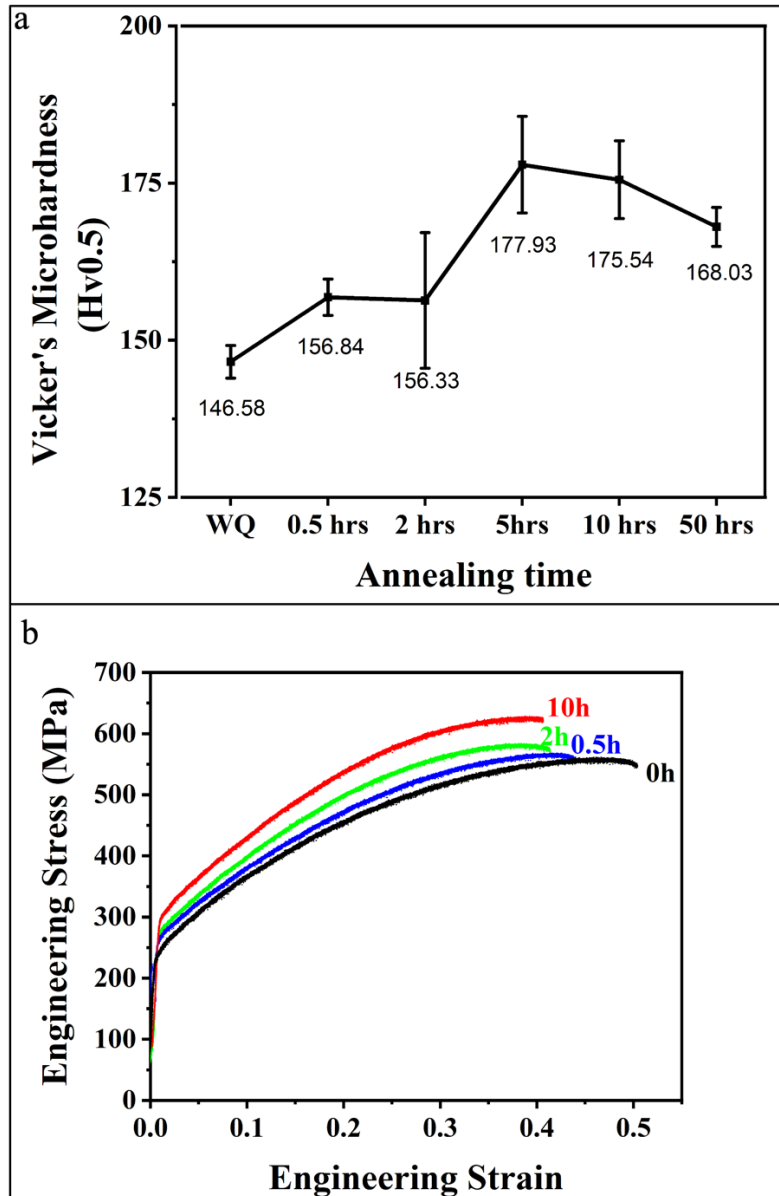


Figure 10: (a) Vicker's microhardness measurements for 500C/X conditions (x=0, 0.5, 2, 5, 10, 50 hrs) (b) Tensile stress-strain curves for 500C/X conditions (x=0, 0.5, 2, 10 hrs)

Tensile stress-strain curves of alloys corresponding to these conditions, shown in Fig. 10(b), reveal a progressive increase in yield strength with increasing annealing time from 0 hours to 10 hours without any significant change in grain size. As discussed previously in case of the microhardness, the observed increase in yield stress with annealing time can also be attributed to the formation of well-developed  $L1_2$  precipitates, from the transient  $L1_2$  nanodomains, which in turn arise from the

Ni-Al rich compositional fluctuations. The subtle increase in yield stress from 0 hrs to 0.5 hrs to 2 hrs results from an increase in the number density of transient L1<sub>2</sub> nanodomains, without the formation of any appreciable fraction of well-developed ordered L1<sub>2</sub> precipitates. Beyond 2 hrs, there is a more rapid increase in yield stress due to the formation of greater fractions of well-developed ordered L1<sub>2</sub> precipitates. It is interesting to note that while the microhardness is similar for 0.5 hrs and 2 hrs conditions (or marginally lower), the yield stress for the latter is marginally higher. This seemingly inconsistent trend is due to the size scale of the testing method in terms of the sampling volume. In microhardness measurements, the sampling volume is limited to  $2.5 \times 10^{-5} \text{ mm}^3$  (assuming 60  $\mu\text{m}$  diameter). The statistical fluctuations associated with the formation of a limited number of well-developed L1<sub>2</sub> precipitates in case of the 500°C/2 hrs annealed sample lead to higher error bars but an overall similar (or marginally lower) microhardness value as compared to the 0.5 hrs annealed sample. On the other hand, the tensile properties measured over  $\sim 5 \text{ mm}^3$  sampling volume, are expected to be uniformly impacted by the presence of these well-developed L1<sub>2</sub> precipitates in case of the 2 hrs annealed condition, leading to a marginally higher value as compared to the 0.5 hrs annealed condition. Subsequently, there is a more pronounced increase in yield stress between 2 hrs to 10 hrs of annealing at 500°C, which can be attributed to further nucleation and growth of the well-developed near-equilibrium L1<sub>2</sub> precipitates.

The formation of L1<sub>2</sub> or  $\gamma'$  phase in the FCC or  $\gamma$  matrix of Ni base superalloys is a widely known precipitation reaction employed for enhancing the mechanical properties. The mechanism of this precipitation reaction, while largely attributed to classical nucleation and growth, can also result from concurrent spinodal decomposition and chemical ordering<sup>33</sup>. Additionally, it has also been proposed that at large undercoolings below the solutionizing temperature (single FCC phase field),

non-classical nucleation of  $L1_2$  or  $\gamma'$  precipitates can occur, with compositions far-from equilibrium<sup>34</sup>. The current manuscript discusses such a non-classical formation of  $L1_2$  precipitates with a far-from equilibrium composition, in the quenched  $Al_{0.25}CoFeNi$  HEA, where the Al has been intentionally added to promote ordering. However, as compared to Ni base superalloys, the principal difference in case of the  $Al_{0.25}CoFeNi$  HEA lies in the fact that the  $L1_2$  precipitates compete with a different ordered B2 phase during the precipitation process. The substantially lower nucleation barrier of  $L1_2$  versus B2, within the FCC matrix, promotes the rapid formation of the former phase while the latter ordered B2 phase precipitation is largely confined to FCC grain boundaries, which act as favorable heterogeneous nucleation sites lowering the nucleation barrier. Such a competition between  $L1_2$  and B2 ordered phases precipitating within the same FCC matrix is not encountered in case of Ni base superalloys.

## 5. Conclusions

In summary, while the equilibrium phases in  $Al_{0.25}CoFeNi$  at 500°C are  $L1_2$  and B2 as predicted by solution thermodynamic modeling (ThermoCalc in the present paper), the homogeneous nucleation and growth of the B2 phase was severely limited due to its high nucleation barrier within FCC matrix. Therefore, the microstructure after 500°C/50 hrs annealing was found to be dominated by homogeneous  $L1_2$  precipitation within the FCC matrix, with limited grain boundary nucleation of either B2 precipitates or small scale B2+BCC colonies. Interestingly, the formation of transient  $L1_2$  phase was observed before near-equilibrium  $L1_2$  precipitation takes place. The transient  $L1_2$  with far-from equilibrium composition is formed from ordering of pre-existing Ni-Al rich regions in the solutionized condition. Subsequently,  $L1_2$  precipitates exhibiting near-equilibrium compositions form within the FCC solid solution mediated by large amplitude

compositional fluctuations. An outcome of these competing pathways is the co-existence of both types of  $L1_2$  (transient and near-equilibrium) in case of some annealed conditions, such as the 500°C/2hrs condition in the present case. Both types of  $L1_2$  phases, transient and near-equilibrium, enhanced the microhardness and tensile yield stress of the  $Al_{0.25}CoFeNi$  HEA, with the near-equilibrium ordered precipitates playing a more dominant role.

### **Supplementary Material**

See supplementary material for the APT raw ion maps from 500°C-30 min condition in Figs. S1(a-d), 500°C-2 hrs condition in Figs. S1(e-h), 500°C-10 hrs condition in Figs. S2(a-d), and 500°C-50 hrs condition in Figs. S2(e-h).

### **Acknowledgements**

The work was supported by the US Air Force Office of Scientific Research under grant FA9550-17-1-0395. This research used resources of the Advanced Photon Source, a U.S. Department of Energy (DOE) Office of Science user facility operated for the DOE Office of Science by Argonne National Laboratory under Contract No. DE-AC02-06CH11357. The authors would also like to acknowledge the staff at Advanced Photon Source, and Materials Research Facility (MRF) at the University of North Texas for use of microscopy facilities.

### **CRedit Statement**

R.B. designed and supervised the research; S.D. and A.C. conducted SEM, APT experiments, and mechanical testing; A.S. conducted TEM analysis; SGS performed computational calculations. S.D. and R.B. wrote the manuscript.

### **Conflict of Interests**

The authors have no conflicts to disclose.

## Data Availability

The data that support the findings of this study are available from the corresponding author upon reasonable request.

## References

- <sup>1</sup> J.P. Couzinié, M. Heczko, V. Mazánová, O.N. Senkov, M. Ghazisaeidi, R. Banerjee, and M.J. Mills, “High-temperature deformation mechanisms in a BCC+B2 refractory complex concentrated alloy,” *Acta Mater.* **233**, 117995 (2022).
- <sup>2</sup> A. Sharma, B. Gwalani, S. Dasari, D. Choudhuri, Y.J. Chang, S. Gorsse, A.C. Yeh, and R. Banerjee, “Insights into Defect-Mediated Nucleation of Equilibrium B2 Phase in Face-Centered Cubic High-Entropy Alloys,” *JOM*, (2021).
- <sup>3</sup> W. Zhang, Y.M. Jin, and A.G. Khachaturyan, “Phase field microelasticity modeling of heterogeneous nucleation and growth in martensitic alloys,” *Acta Mater.*, (2007).
- <sup>4</sup> W.X. Zhao, S.H. Jiang, W.H. Liu, X.Y. Peng, H. Wang, Y. Wu, X.J. Liu, and Z.P. Lu, “Synergistic effects of microalloying and pre-straining on enhanced nanoprecipitation and creep property of alumina-forming austenitic stainless steels,” *Mater. Sci. Eng. A*, (2022).
- <sup>5</sup> B. Gwalani, S. Gorsse, D. Choudhuri, M. Styles, Y. Zheng, R.S. Mishra, and R. Banerjee, “Modifying transformation pathways in high entropy alloys or complex concentrated alloys via thermo-mechanical processing,” *Acta Mater.* **153**, 169–185 (2018).
- <sup>6</sup> M. Laver, B.J. Connolly, C. Cooper, J. Kohlbrecher, S. Samothrakitis, and K. Wilford, “Characterizing accelerated precipitation in proton irradiated steel,” *J. Nucl. Mater.*, (2021).
- <sup>7</sup> J.L. Bocquet, and G. Martin, “Irradiation-induced precipitation: A thermodynamical approach,” *J. Nucl. Mater.*, (1979).
- <sup>8</sup> F. Soisson, and T. Jourdan, “Radiation-accelerated precipitation in Fe-Cr alloys,” *Acta Mater.*, (2016).
- <sup>9</sup> T. Yang, W. Guo, J.D. Poplawsky, D. Li, L. Wang, Y. Li, W. Hu, M.L. Crespillo, Z. Yan, Y. Zhang, Y. Wang, and S.J. Zinkle, “Structural damage and phase stability of Al<sub>0.3</sub>CoCrFeNi high entropy alloy under high temperature ion irradiation,” *Acta Mater.* **188**, 1–15 (2020).
- <sup>10</sup> Y. Wang, and J. Li, “Phase field modeling of defects and deformation,” *Acta Mater.*, (2010).
- <sup>11</sup> I.A. Tomilin, and S.D. Kaloshkin, “‘High entropy alloys’—‘semi-impossible’ regular solid solutions?,” *Mater. Sci. Technol.* **31**(10), 1231–1234 (2015).
- <sup>12</sup> M. Widom, “Modeling the structure and thermodynamics of high-entropy alloys,” *J. Mater. Res.*, (2018).
- <sup>13</sup> B. Cantor, I.T.H. Chang, P. Knight, and A.J.B. Vincent, “Microstructural development in equiatomic multicomponent alloys,” *Mater. Sci. Eng. A*, (2004).
- <sup>14</sup> J.W. Yeh, S.K. Chen, S.J. Lin, J.Y. Gan, T.S. Chin, T.T. Shun, C.H. Tsau, and S.Y. Chang, “Nanostructured high-entropy alloys with multiple principal elements: Novel alloy design concepts and outcomes,” *Adv. Eng. Mater.* **6**(5), 299–303 (2004).
- <sup>15</sup> S. Singh, N. Wanderka, B.S. Murty, U. Glatzel, and J. Banhart, “Decomposition in multi-component AlCoCrCuFeNi high-entropy alloy,” *Acta Mater.* **59**(1), 182–190 (2011).

- <sup>16</sup> S. Dasari, A. Jagetia, A. Sharma, M.S.K.K.Y. Nartu, V. Soni, B. Gwalani, S. Gorsse, and R. Banerjee, “Tuning the degree of chemical ordering in the solid solution of a complex concentrated alloy and its impact on mechanical properties,” *Acta Mater.* **212**, 116938 (2021).
- <sup>17</sup> Y. Tong, D. Chen, B. Han, J. Wang, R. Feng, T. Yang, C. Zhao, Y.L. Zhao, W. Guo, Y. Shimizu, C.T. Liu, P.K. Liaw, K. Inoue, Y. Nagai, A. Hu, and J.J. Kai, “Outstanding tensile properties of a precipitation-strengthened FeCoNiCrTi0.2 high-entropy alloy at room and cryogenic temperatures,” *Acta Mater.* **165**, 228–240 (2019).
- <sup>18</sup> P. Shi, W. Ren, T. Zheng, Z. Ren, X. Hou, J. Peng, P. Hu, Y. Gao, Y. Zhong, and P.K. Liaw, “Enhanced strength–ductility synergy in ultrafine-grained eutectic high-entropy alloys by inheriting microstructural lamellae,” *Nat. Commun.* **10**(1), 1–8 (2019).
- <sup>19</sup> D.B. Miracle, and O.N. Senkov, “A critical review of high entropy alloys and related concepts,” *Acta Mater.* **122**, 448–511 (2017).
- <sup>20</sup> T. Yang, Y.L. Zhao, Y. Tong, Z.B. Jiao, J. Wei, J.X. Cai, X.D. Han, D. Chen, A. Hu, J.J. Kai, K. Lu, Y. Liu, and C.T. Liu, “Multicomponent intermetallic nanoparticles and superb mechanical behaviors of complex alloys,” *Science* (80-. ). **362**(6417), 933–937 (2018).
- <sup>21</sup> Y.J. Liang, L.L. Wang, Y. Wen, B. Cheng, Q. Wu, T. Cao, Q. Xiao, Y. Xue, G. Sha, Y. Wang, Y. Ren, X. Li, L.L. Wang, F. Wang, and H. Cai, “High-content ductile coherent nanoprecipitates achieve ultrastrong high-entropy alloys,” *Nat. Commun.* **9**(1), 1–8 (2018).
- <sup>22</sup> J.Y. He, H. Wang, H.L. Huang, X.D. Xu, M.W. Chen, Y. Wu, X.J. Liu, T.G. Nieh, K. An, and Z.P. Lu, “A precipitation-hardened high-entropy alloy with outstanding tensile properties,” *Acta Mater.* **102**, 187–196 (2016).
- <sup>23</sup> S. Dasari, B. Gwalani, A. Jagetia, V. Soni, S. Gorsse, and R. Banerjee, “Hierarchical Eutectoid Nano-lamellar Decomposition in an Al0.3CoFeNi Complex Concentrated Alloy,” *Sci. Rep.* **10**, 4836 (2020).
- <sup>24</sup> A. Takeuchi, and A. Inoue, “Classification of bulk metallic glasses by atomic size difference, heat of mixing and period of constituent elements and its application to characterization of the main alloying element,” *Mater. Trans.* **46**(12), 2817–2829 (2005).
- <sup>25</sup> L.T. Stephenson, M.P. Moody, P. V. Liddicoat, and S.P. Ringer, in *Microsc. Microanal.* (2007), pp. 448–463.
- <sup>26</sup> J.M. Hyde, E.A. Marquis, K.B. Wilford, and T.J. Williams, “A sensitivity analysis of the maximum separation method for the characterisation of solute clusters,” *Ultramicroscopy* **111**(6), 440–447 (2011).
- <sup>27</sup> A. Fantin, G.O. Lepore, A.M. Manzoni, S. Kasatkov, T. Scherb, T. Huthwelker, F. d’Acapito, and G. Schumacher, “Short-range chemical order and local lattice distortion in a compositionally complex alloy,” *Acta Mater.*, (2020).
- <sup>28</sup> X. Chen, Q. Wang, Z. Cheng, M. Zhu, H. Zhou, P. Jiang, L. Zhou, Q. Xue, F. Yuan, J. Zhu, X. Wu, and E. Ma, “Direct observation of chemical short-range order in a medium-entropy alloy,” *Nature* **592**(7856), 712–716 (2021).
- <sup>29</sup> A. Fernández-Caballero, J.S. Wróbel, P.M. Mummery, and D. Nguyen-Manh, “Short-Range Order in High Entropy Alloys: Theoretical Formulation and Application to Mo-Nb-Ta-V-W System,” *J. Phase Equilibria Diffus.* **38**, 391–403 (2017).
- <sup>30</sup> C.G. Schön, “On short-range order strengthening and its role in high-entropy alloys,” *Scr. Mater.* **196**, (2021).
- <sup>31</sup> O.C. Hellman, J.A. Vandenbroucke, J. Rüsing, D. Isheim, and D.N. Seidman, “Analysis of three-dimensional atom-probe data by the proximity histogram,” *Microsc. Microanal.* **6**(5), 437–444 (2000).

<sup>32</sup> D.A. Porter, K.E. Easterling, and M.Y. Sherif, *Phase Transformations in Metals and Alloys, Third Edition* (2009).

<sup>33</sup> D.M. Collins, N. D'Souza, C. Panwisawas, C. Papadaki, G.D. West, A. Kostka, and P. Kontis, "Spinodal decomposition versus classical  $\gamma'$  nucleation in a nickel-base superalloy powder: An in-situ neutron diffraction and atomic-scale analysis," *Acta Mater.*, (2020).

<sup>34</sup> W.A. Soffa, and D.E. Laughlin, "Decomposition and ordering processes involving thermodynamically first-order order  $\rightarrow$  disorder transformations," **37**(11), 3019–3028 (1989).